Triplet dynamics in fluorescent polymer light-emitting diodes

Bodo H. Wallikewitz,* Dinesh Kabra, Simon Gélinas, and Richard H. Friend†

University of Cambridge, Optoelectronics Group, Cavendish Laboratory, JJ Thomson Ave., Cambridge CB3 0HE, United Kingdom

(Received 26 August 2011; revised manuscript received 1 December 2011; published 17 January 2012)

We report a study of the triplet exciton dynamics and their effect on the performance of fluorescent organic light-emitting diodes. These polymer light-emitting diodes comprise metal oxide, injection electrodes, and poly(9,9′-dioctylfluorene-co-benzothiadiazole) as the emissive material and exhibit external quantum efficiencies up to 6.5%. Transient optical absorption measurements following a short (0.5 to 50 μs) electrical drive pulse were used to monitor triplet dynamics during device operation. Triplet generation and decay processes were modeled, and we find that triplet-triplet annihilation is the dominant triplet decay mechanism. Singlet states, generated from triplet-triplet annihilation were monitored as delayed electroluminescence after the end of the drive pulse. From the delayed electroluminescence dynamics, we determine monomolecular as well as bimolecular triplet decay rates and estimate the triplet-charge annihilation rate. Singlet states generated from bimolecular triplet-triplet annihilation contribute up to 33% of the total amount of singlets generated in these fluorescent devices. To model these results, we require that triplet states can undergo bimolecular annihilation several times. With this model, we show that singlets can reach a maximum fraction of 40% of all excitons generated by charge recombination, without violating spin statistics. Singlet states generated from triplet-triplet annihilation are one important explanation for high external quantum efficiencies found in these fluorescent devices.

DOI: 10.1103/PhysRevB.85.045209 PACS number(s): 81.05.Fb, 78.47.da, 85.60.Jb, 33.50.−j

I. INTRODUCTION

In fluorescent organic light-emitting diodes (OLEDs), light emission comes from singlet excitons,[1–3] representing only 25% of the total exciton population if electron-hole capture is independent of spin and thus limiting the device efficiency.[4,5] A milestone for the improvement of brightness and efficiency of OLEDs was the introduction of phosphorescent emitters, raising the fraction of emissive excitons up to 100% by incorporating triplets in the emission process.[6,7] The generation of dopant triplets via intersystem crossing from host singlets introduces a ∼0.7 eV exchange energy loss.[5] This loss process reduces the power efficiency, raises the injection barrier for charges, and is disadvantageous for the efficiency and stability, in particular, of blue phosphorescent devices.[7,8] The absence of these losses makes fluorescent emitters more favorable in the blue spectral region. Optimized devices containing fluorescent emitters can be superior to their phosphorescent counterparts, as demonstrated in highly efficient, white OLEDs.[7,8] Furthermore, there have been reports of significant improvements in external quantum efficiency (EQE) of fluorescent OLEDs, up to 7.3 and 11% EQE, exceeding theoretical limitations.[9,10] This demonstrates the need for fundamental investigations in order to better understand fluorescent emitters and thereby to unlock their potential for highly efficient OLEDs.

The EQE (η_{ext}) is a measure of the yield of emitted photons in forward direction per injected electron. For an efficient generation of emissive excitons from charges, a balanced ratio of electrons and holes must be injected and transported through the device, described by γ, the charge balance ratio. The recombination of charges to singlets is limited by spin statistics (η_{spin}), resulting in the generation of 25% singlets and 75% triplets.[5] The maximum yield of photons generated per singlet is then given by the photoluminescence quantum yield (PLQE) φ. From the total amount of photons generated in the emissive layer, only a fraction η_{out} is coupled out through the surface. The determination of absolute values for η_{spin}, γ, and η_{out} is outside the scope of this paper. We assume $\eta_{out} = 0.2$ for the device geometry used in this study.[11] Using a value of 75% for the PLQE of poly(9,9′-dioctylfluorene-co-benzothiadiazole) (F8BT),[9] assuming perfect charge balance and generation of 25% singlets, we estimate the upper limit of the EQE to be $\eta_{ext} = \varphi\ \gamma\ \eta_{spin}\ \eta_{out} \sim 3.75\%$. To understand the deviation of the EQEs from this modeled limit, we present a detailed study of excited state dynamics in this paper.

We investigate the dynamics of excited states, generated by an electrical drive pulse, by applying transient optical absorption (TA) spectroscopy to working devices. This is in contrast to most studies of excited-state dynamics that were carried out on photoexcited thin films.[12,13] With TA spectroscopy, we can detect several excited states simultaneously by their characteristic absorption features in a broad spectral range from visible to infrared. Further advantages of TA spectroscopy include a high time resolution and high sensitivity for detection of excited states. Previously, single wavelength TA measurements have been reported for electrically driven OLEDs, where it was used to measure singlet-to-triplet ratios and to investigate generation and decay processes at low temperatures.[14–17]

Another technique to study excited state processes is time-resolved photo luminescence (PL) spectroscopy. It has been used to study photogenerated, delayed fluorescence originating from bimolecular triplet-triplet annihilation[5,15,18] and from recombination of geminate electron-hole pairs.[19,20] However, delayed emission following electrical excitation has been less investigated. Delayed electroluminescence has been attributed to residual charges after switch-off of an electrical driving pulse,[20,21] to emissive singlet states formed by triplet-triplet annihilation,[10,17,22–25] and to slow recombination of detrapped charges.[25,26] A contribution of up to ∼50% delayed to steady-state electroluminescence (EL) intensity provides evidence for its strong contribution to steady-state brightness and efficiency.[10] Thus high EQEs in fluorescent

OLEDs have been explained by the contribution of singlets generated from triplet-triplet annihilation to the overall singlet density.[10,17,22–25]

In the present investigation, we study single layer, polymer light-emitting diodes (PLEDs) fabricated with F8BT as the emissive layer. We have recently reported that when these devices are constructed with metal oxide charge-injection electrodes, they can show extremely high efficiencies, up to 23 cd/A for this yellow-green emissive material, corresponding to EQE in the forward direction of 7.3%.[9] In these hybrid structures, the F8BT layer is sandwiched between a solution processed, ZnO/Cs_2CO_3 electron-injection layer and a top, thermally evaporated MoO_3/Au hole-injection layer.[9] The semiconducting polymer F8BT used as active layer has been studied previously regarding its photophysical, thin film properties using quasi-continuous wave (CW) photoinduced absorption (PIA) spectroscopy. Dhoot *et al.* and Ford *et al.* have reported mono- and bimolecular triplet decay rates for F8BT.[27,28] Lee *et al.* experimentally confirmed a previously calculated triplet-triplet absorption cross-section $\sigma_{abs}(T)$, at 800 nm of 3.1×10^{-16} cm^2 (note that this quantity is needed to calculate triplet densities from transient absorption measurements).[29]

To understand the high efficiency of the studied hybrid PLEDs, we investigated excited state dynamics on working devices by TA spectroscopy and transient EL measurements. Emissive and nonemissive excited states are monitored by their characteristic absorption features using transient absorption spectroscopy. In contrast, only emissive states are detected via time-resolved EL measurements to provide information about related, nonemissive states. By fitting a model for triplet decay to the experimental triplet and EL dynamics, we are able to quantitatively characterize the various triplet decay processes. From these results, we conclude that triplet-triplet annihilation is the dominant triplet decay mechanism. We experimentally prove a strong generation of singlets by triplet-triplet annihilation and confirm its contribution to the device efficiency, which is in agreement with our triplet decay model. Excited state dynamics are measured for various current densities up to 30 A/cm^2, where we find a strong decrease of the fraction of singlets generated from triplet-triplet annihilation compared to the total fraction of singlets. We explain this reduction by triplet-charge annihilation.

The content of this paper is structured as follows: Experimental details are given in Sec. II. In Secs. III A and III B, a model for triplet decay processes and their contribution to singlet exciton generation is developed. We present the results of device characterizations in Sec. IV A, of transient EL measurements in Sec. IV B and of TA measurements in Sec. IV C. The triplet decay mechanism is characterized and discussed in Sec. V A, and its contribution to the device efficiency is presented in Sec. V B. Loss processes of triplets at high current densities are discussed in Sec. V C. Conclusions are given in Sec. VI. In the Appendix, a model for triplet generation is provided.

II. EXPERIMENTAL METHODS

PLEDs were made with a F8BT thickness of (1 ± 0.1) μm as described in previous publications.[9,30] Direct current-(dc)-voltage-luminance measurements were performed using a Keithley 2400 sourcemeter, a calibrated photodiode, and a Keithley picoamperemeter 2000. For pulsed driving, a home-made amplifier, driven by an Agilent 8116A function generator was used. The pulsed current-voltage-luminance characteristics were measured with an induction current probe and a photomultiplier tube using an Agilent DSO80304B 3 GHz oscilloscope. For time-resolved TA and EL measurements, the PLEDs were driven in pulse mode with a frequency of 500 Hz and a pulse length of 0.5–50 μs. For time-resolved EL measurements, an intensified charge-coupled device (ICCD, Andor IStar) was used as detector. The gate width and integration time was varied depending on the delay time.

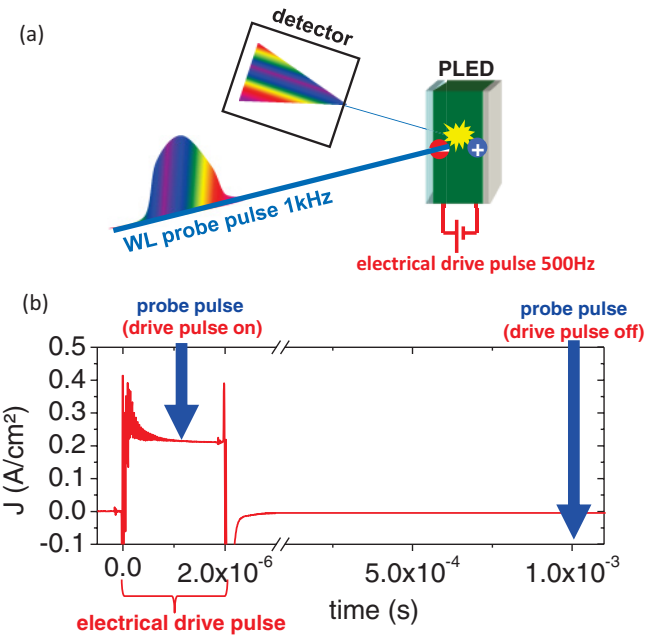

FIG. 1. (Color online) (a) Schematic picture of the PLED transient absorption measurement setup. The white-light (WL) probe pulse (blue line) is reflected on the back electrode of the PLED into the detector to measure the transmitted intensity. The differential transmission ΔT is obtained by measuring the signal with and without electrically generated excited states, using a probe (blue arrow) with a frequency of 1 kHz, twice the frequency of the electrical drive pulse (red line). The timing of the drive (red line) and probe pulses (blue arrow) is shown in (b).

The experimental setup for TA measurements on PLEDs is shown in Fig. 1. The short (100 fs) white-light (WL) probe pulses generated by a Ti-sapphire laser system described elsewhere[31] are transmitted through the PLED and reflected from the back electrode into the detector [Fig. 1(a)]. WL probe pulses from 520 nm to 780 nm and from 805 nm to 950 nm were used in two separate measurements to cover the spectral range, over which different excited states absorb. The gap around 800 nm is due to the exclusion of the fundamental of the Ti-sapphire oscillator to maintain high WL stability. The timing of the electrical drive and optical probe pulse is shown in Fig. 1(b). To determine the differential transmission $\Delta T = T_{off} - T_{on}$, the frequency of the WL probe pulse [blue arrow, Fig. 1(b)] is chosen to be 1 kHz. This allows the comparison of the transmittance in absence of excited states (T_{off}) and in

their presence (T_{on}) [red line, Fig. 1(b)], as the drive pulse has a frequency of 500 Hz.

By delaying the electrical pulse with respect to the WL probe pulse using a delay generator (Stanford Research Instruments, DG 535), it is possible to measure the build-up and decay dynamics of excited states during and after the drive pulse with a time resolution as low as 0.5 ns. The TA experiment has a resolution for fractional change in transmission of 2×10^{-5}. With a thickness $d = 1\mu$m and the cross-section of excited state absorption $\sigma = 2\times10^{-16}$ cm^{-2}, excited state densities n as low as $\sim10^{15}$ cm^{-3} can be detected, according to $n = \Delta T/T/d/\sigma$.

III. MODEL FOR TRIPLET EXCITON DYNAMICS

A. Triplet decay processes

Triplet excitons are the dominant excited states in OLEDs due to a threefold higher generation rate compared to singlet states according to spin statistics.[5,32–34] Their long lifetime in the range of microsecond to millisecond results in the accumulation of triplet states and the rise of their density during the drive pulse. This leads to orders of magnitude higher triplet densities compared to singlet densities, as singlets have a lifetime in the picosecond to nanosecond range. Monomolecular and bimolecular processes contribute to triplet decay. Bimolecular triplet-triplet collision (TTC) is a diffusion-limited process with the collision of two triplets leading to an intermediate state with twice the energy of the T_1 state. Of the possible intermediate states, comprising one singlet, three triplet, and five quintet states, the quintet states are generally expected to be higher in energy than the two triplets,[5] so the intermediate state then relaxes to either an excited triplet state T_n that rapidly relaxes to the T_1 triplet, Eq. (1a) or to a singlet state S_1, Eq. (1b).

$$T_1 + T_1 \rightarrow \mathrm{T}_n + S_0(\rightarrow T_1 + S_0), \tag{1a}$$

or

$$T_1 + T_1 \rightarrow S_1 + S_0. \tag{1b}$$

The fraction f of S_1 singlets formed following a single TTC event is thus expected to be 25%. The fraction f has an important influence on the device physics, as it limits the fraction of singlets generated from each TTC event. However, the T_1 states formed by Eq. (1a) can themselves be recycled in further TTC reactions, so, if no other decay channels are present, the maximum fraction of singlets from this series of TTC processes, f_∞ is given by Eq. (2a)

$$f_\infty = \frac{f}{2}\sum_{n=0}^{n=\infty}\left(\frac{1-f}{2}\right)^n = f\frac{1-f}{1+f}. \tag{2a}$$

For $f = 25\%$ we obtain $f_\infty = 15\%$, so including the initial generation of singlets, the maximum singlet fraction is $25\% + 15\% = 40\%$, and the fraction regenerated via TTC $= 15\%/(15\% + 25\%) = 37.5\%$. A schematic picture of this model is shown in Fig. 2. The contribution of singlets from TTC to the device efficiency will be discussed and confirmed by experimental results in this article (Secs. IV and V).

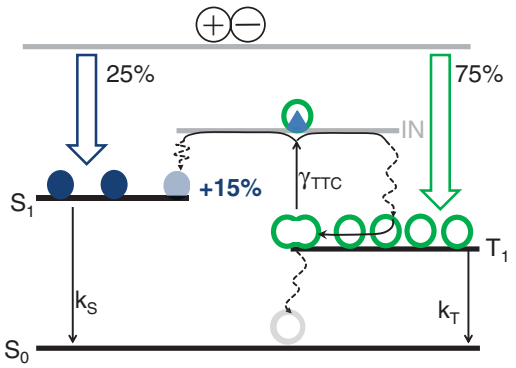

FIG. 2. (Color online) Schematic picture of the generation and decay paths of singlet and triplet states. From charge recombination (thick arrows), 25% singlets (S_1, blue, filled circles) and 75% triplets (T_1, green, open circles) are generated according to spin statistics. During triplet-triplet collison (TTC) with the rate constant γ_{TTC}, one of the triplets undergoes a nonradiative transition to the ground state (S_0, grey, open circle), while the other one forms a higher lying intermediate (IN) state with 1/4 singlet and 3/4 triplet character (quater-filled, green circle). Assuming that triplets can underdo collision several times [Sec. III A, Eq. (2a)], TTC can generate an additional fraction of maximum 15% singlets (light blue, filled circle). Alternative, monomolecular decay of singlets and triplets with the rate constants k_S and k_T is shown by vertical arrows.

We define the bimolecular collision rate at γ_{TTC} and distinguish this from the bimolecular annihilation rate for triplet excitons, γ_{TT} given by

$$\gamma_{TT} = \gamma_{TTC}\frac{1-f}{2}. \tag{2b}$$

In addition to bimolecular triplet-triplet annihilation with the rate γ_{TT}, we allow triplets to undergo monomolecular decay at a rate k_T. We now consider the triplet dynamics after the end of the drive pulse, when the generation is switched off. We assume a spatially invariant triplet density [T] for this simplified model, which is represented by Eq. (3a), and its analytical solution is given by Eq. (3b)[35]

$$\frac{d[T]}{dt} = -k_T[T(t)] - \gamma_{TT}[T(t)]^2, \tag{3a}$$

$$[T] = \frac{T_0\exp(-k_T t)}{1+\frac{T_0\gamma_{TT}}{k_T}\left[1-\exp(-k_T t)\right]}. \tag{3b}$$

At low triplet densities $n_T\gamma_{TT} \ll k_T$ monomolecular decay is dominant, and at high triplet densities $n_T\gamma_{TT} \gg k_T$ triplet-triplet annihilation is the dominant decay process. The transition between the two regimes can be estimated as $\sim k_T/\gamma_{TT} \sim 10^{15}$ cm^{-3}, using values of $k_T \sim 10^4$/s and $\gamma_{TT} \sim 10^{-11}$ cm^3/s obtained below in Sec. V A. This shows that triplet-triplet annihilation is the dominant decay process in the detection range $n_T > 10^{15}$ cm^{-3} of the TA experiment. In this case, k_T is neglected and excluded from Eq. (3a), resulting in the rate Eq. (4a) with the analytical solution (4b)

$$\frac{d[T]}{dt} = -\gamma_{TT}[T(t)]^2, \tag{4a}$$

$$[T] = \frac{T_0}{(1+\gamma_{TT}T_0 t)}. \tag{4b}$$

Assuming that the encounter of two triplet states during triplet-triplet annihilation forms a fraction f of emissive singlet states, the intensity of delayed EL $I_{\mathrm{EL}} \propto \frac{1}{2} f \gamma_{\mathrm{TTC}} T^2$. Using Eq. (3b) to represent the triplet density for delayed EL measurements, we obtain:

$$I(\mathrm{EL}) = A\frac{1}{2} f \gamma_{\mathrm{TTC}} T^2 = A\frac{f}{(1-f)}\gamma_{TT}\left[\frac{T_0 \exp(-k_T t)}{1+\frac{T_0\gamma_{TT}(\mathrm{EL})}{k_T}\left[1-\exp(-k_T t)\right]}\right]^2. \quad (5)$$

The initial triplet density T_0 shortly after the end of the pulse is derived from device TA measurements. Deviation of absolute decay rates from measurements of relative EL intensities is possible, when absolute triplet densities T_0 are used in Eq. (5). In order to combine absolute T_0 values with relative EL intensities, the constant of proportionality A is introduced in Eq. (5).

B. Charge density and charge transport

One of the processes that can contribute to monomolecular triplet decay is that of triplet-charge collision. We need therefore to model the distribution and density of injected charges under device operation. We have recently reported that the current-voltage characteristics of the bipolar PLEDs used here are very similar to the characteristics of unipolar hole-only devices because hole injection and transport is easier than for electrons in these devices, and electron-hole capture takes place close to the cathode.[9] Hence, we use a similar hole space-charge distribution. This model is realistic for other hole-only and bipolar devices with polyfluorene as active material.[36] The space-charge zone of the holes in our PLEDs reaches from the injecting MoO_3 anode up to the recombination zone, which is close to the cathode. The unipolar field dependent space-charge limited current (SCLC) model presented in Eq. (6) is fitted to the experimental current-voltage characteristics using

$$J = \frac{9}{8}\varepsilon\varepsilon_0\mu_0\frac{V^2}{d^3}e^{(\beta\sqrt{\frac{V}{d}})}. \quad (6)$$

In Eq. (6) the zero-field mobility μ_0 and the field dependency β are free parameters at a fixed film thickness d.[37,38]

In the presence of SCLC, the distribution of holes in the space-charge zone is then described by Eq. (7)

$$n_c(x) = \frac{3}{4}\frac{\varepsilon\varepsilon_0 V}{ed^2}\sqrt{\frac{d}{x}}. \quad (7)$$

The charge density $n_c(x)$ is dependent on the voltage V and on the position in the film x between the anode ($x = 0$) and the cathode ($x = \mathrm{d}$). For a more complete model of charge transport in unipolar OLEDs, we refer the reader to Paseveer *et al.*.[39]

As the hole density can have an effect on the triplet decay, we need a description of its density profile. Indeed, holes in our devices can annihilate with triplets in a bimolecular reaction and cause a transition of triplets to the ground state, while the excess energy is transferred to the hole. This loss of triplets is reflected in the charge density-dependent triplet decay rate $k_T(n_c)$. It is described by Eq. (8) as a combination of the unperturbed monomolecular triplet decay in absence of charges with the rate k_0 and the triplet-charge annihilation with the rate γ_{TC}:

$$k_T(n_C) = k_0 + \gamma_{TC}[n_C]. \quad (8)$$

From the charge- and triplet-density profiles, we can estimate the region over which they overlap and interact. The mean charge density $\langle n_c \rangle$ in this region is calculated by integration of Eq. (7) over the region of the film, where interaction of charges with triplets can occur. This region starts at $x = \delta d$, expressed as a fraction δ of the total film thickness and spans up to the cathode ($x = d$). The mean charge density is calculated by Eq. (9)

$$\langle n_c \rangle = \frac{1}{d-\delta d}\int_{x=\delta d}^{x=d} n_c(x)dx = \frac{3}{2}\frac{\varepsilon\varepsilon_0 V}{ed^2}\cdot\frac{1-\sqrt{\delta}}{1-\delta} = \frac{3}{2}\frac{\varepsilon\varepsilon_0 V}{ed^2}\cdot\theta, \quad (9)$$

where $\theta = 1$ for an interaction zone spanning the whole film ($\delta = 0$) and decreases monotonically toward 0.5 when that zone becomes small ($\delta \to 1$). In our case, interaction of triplets and charges occurs within a range of (105 ± 75) nm from the cathode toward the anode. This length is approximately the diffusion length of triplets, as determined in Sec. V A. This results in $\delta = (0.90 \pm 0.07)$ and $\theta = (0.7 \pm 0.2)$.

The relative change in the triplet-decay rate ($\Delta k/k_0$) due to the presence of holes then enables the calculation of the γ_{TC} value by combining Eqs. (8) and (9) to Eq. (10)

$$\frac{\Delta k}{k_0} = \frac{3\gamma_{TC}\varepsilon\varepsilon_0}{2k_0 ed^2}\theta V. \quad (10)$$

The unperturbed monomolecular triplet decay rate k_0 is determined from extrapolation of $k_T(n_c)$ toward zero injection current.[40]

This model is valid once steady-state conditions are reached. The charge distribution in our device is then described by the space-charge zone of dominant holes that reaches from the anode to the cathode. These holes recombine close to the cathode with electrons to form triplets. The model does not consider electron-hole collisions, and we note that the electron density in the device is low as it is only present at the interface F8BT/cathode. Once the pulse ends, the distribution of charges is likely to deviate from the SCLC model, and a time-dependent drift diffusion model would be required to describe accurately the charge distribution. Additionally, deviations of the steady-state charge density from the SCLC model might occur for the following reasons: An electron charge zone can be generated due to field-enhanced, thermionic electron injection at high current densities. This can result in a shift of the recombination zone away from the cathode. Furthermore, charge densities inside the recombination zone might contribute to the triplet-charge annihilation. These contributions are too complex to be considered by the above model. These deviations of the charge density from the SCLC model would directly affect the γ_{TC} value as displayed by Eq. (10). Consequently, only a qualitative estimation of the γ_{TC} value can be calculated.

This model for the decay of triplet states is used to derive the decay rates k_0, $k_T(n_c)$, γ_{TT}, and γ_{TC}, depending on

drive current density J and pulse length τ. This is possible, because we can calculate the triplet densities with $n_T = \Delta T/T/\sigma_{abs}(T)/d$ using the triplet cross-section $\sigma_{abs}(T) = 3.1\times10^{-16}$ cm^2 at 800 nm as measured by Lee *et al.*.[29]

IV. RESULTS

A. Current density-voltage-luminance characteristics of the PLEDs:

The emissive material F8BT has a broad absorption peaking at 460 nm with a tail up to ~575 nm [Fig. 3(a), dashed line]. It overlaps with the yellow-green EL [Fig. 3(a), line] of the PLEDs with the maximum at 565 nm. The efficiency of these PLEDs reaches 22 cd/A with an EQE of 6.5% [Fig. 3(b)], as reported previously.[9] The device layout is shown in Fig. 3(d). The dc and pulsed (pulse length $\tau = 10$ μs) current density-voltage (J-V) characteristics are shown in Fig. 3(c). Evidence for the presence of electric-field-dependent SCLC in the PLEDs is given by the fit of Eq. (6) [Fig. 3(c), line] to the experimental data yielding a typical value of the E-field-dependent factor $\beta = 0.50$ μm$^{0.5}$ $V^{-0.5}$ and the zero-field mobility $\mu_0 = 7\times10^{-6}$ cm^2/V/s.[38]

B. Study of EL dynamics by time-resolved measurements

The prompt EL for $J = 0.2$ A/cm^2 shows an early, fast rise time of ~0.4 μs to reach 80% of the steady-state value, followed by a slow rise until ~10 μs to reach the steady-state level [Figs. 4(a) and 4(b)]. The fast rise is due to the time for charges (holes) to transit the F8BT layer and reach the ZnO cathode, where recombination with electrons takes place to generate emissive singlets.[20,21] It is important to mention that the current reaches its steady-state value at ~500 ns and cannot explain the slow EL rise up to 10 μs.

1. Study of delayed EL dynamics and their contribution to the device efficiency

After the electrical drive pulse is switched off, the EL intensity drops quickly, within a few hundred nanoseconds, to <37.5% of its steady-state value [Figs. 4(b) and 4(d)]. This is followed by a slow decay of the delayed EL for several hundred microseconds (Figs. 4 and 5). We are interested in the intensity of the delayed EL shortly after the pulse end and define R(EL) as its ratio compared to steady-state EL intensity. This ratio strongly depends on current density and pulse length. R(EL) increases at J = 0.2 A/cm^2 with pulse length from R(EL) = 5% for $\tau = 0.5$ μs to R(EL) = 22% for $\tau \geqslant 10$ μs [Figs. 4(b) and 5(c)]. We achieved a significant increase of R(EL) by decreasing the current density to $J = 10$ mA/cm^2. This leads to a maximum value of R(EL) = 33% [Fig. 5(a)], close to the theoretical maximum of R(EL) = 37.5% as described in Sec. III A. The delayed EL is not directly generated by recombination of injected charges and thus forms an additional, strong contribution to the steady-state device brightness. The delayed to steady-state EL intensity ratio is summarized for different pulse length and current densities in Fig. 5(c) and demonstrates the importance of its contribution for steady-state brightness and efficiency.

Figure 5(d) shows that R(EL) decreases from 33 to 8.5% as the current density increases from 0.01 to 30 A/cm^2.

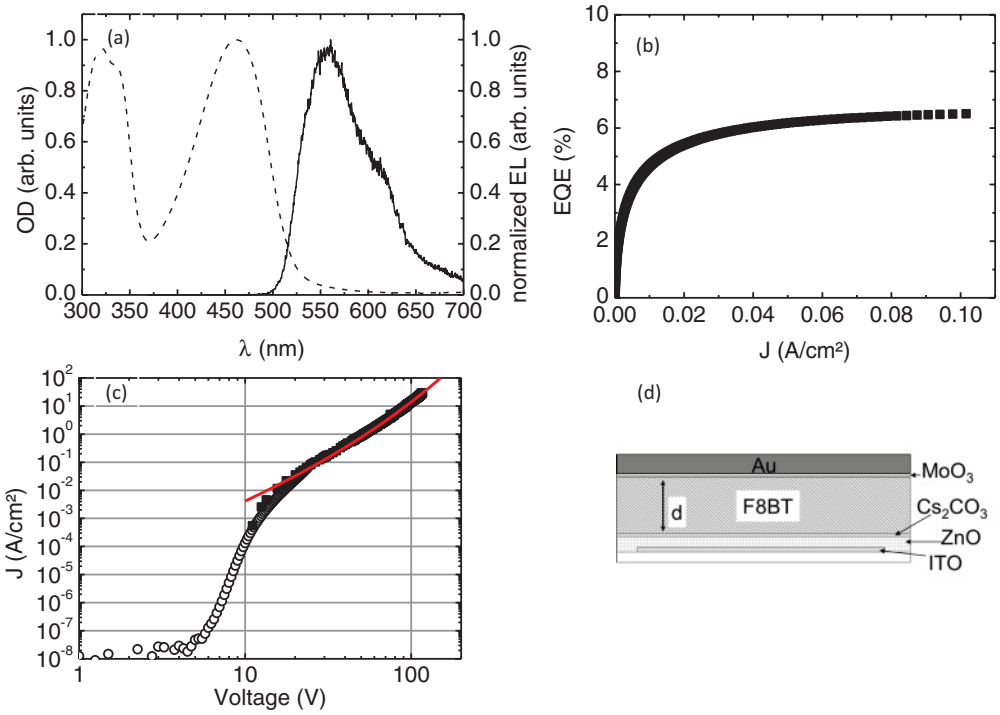

FIG. 3. (Color online) (a) Normalized absorption (dashed line) of a F8BT film and EL (line) of PLEDs. In (b) the EQE is plotted vs the current density. In (c) the dc (open circle) and pulsed (filled squares, pulse length $\tau = 10$ μs) J-V characteristics of PLEDs are shown as well as a fit of the electric-field-dependent SCLC model, Eq. (6) (red line), to the pulsed J-V characteristics. The PLED device structure is shown in (d).

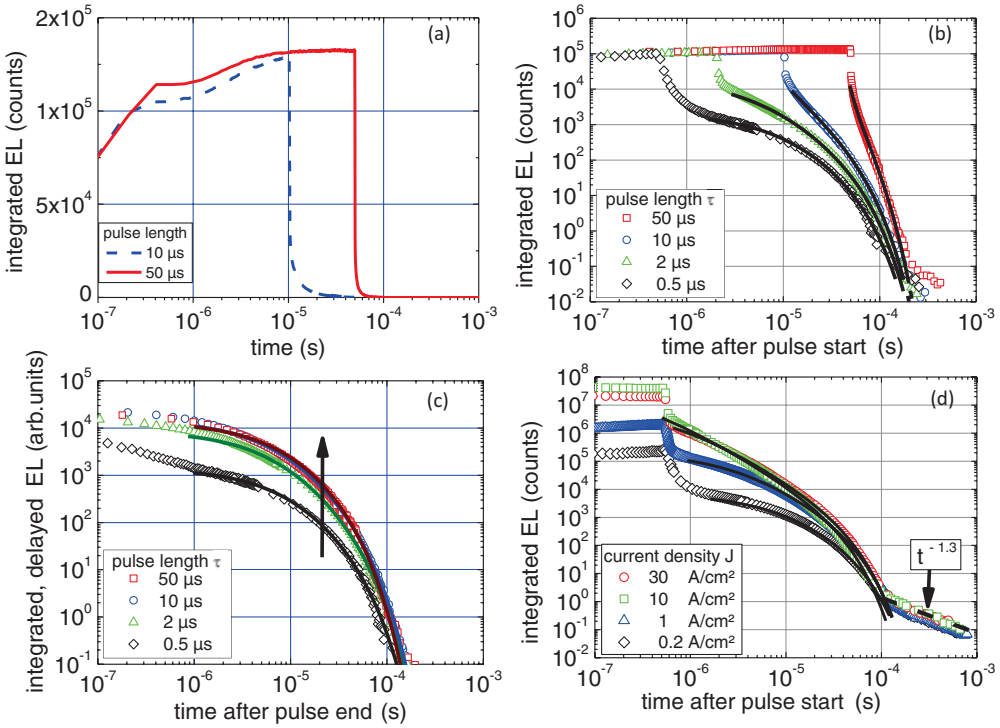

FIG. 4. (Color online) Time-resolved EL data, integrated over the whole EL spectrum of PLEDs, driven at $J = 0.2$ A/cm^2 are presented in (a) in a linear-logarithmic fashion for pulse length of $\tau = 10$ μs (blue, dashed line) and 50 μs (red line) for illustration of the EL rise time. (b) Time-resolved EL data (symbols) are presented in a double logarithmic plot for $\tau = 0.5$ μs (black diamond), 2 μs (green triangle), 10 μs (blue circle), and 50 μs (red square). The triplet decay model, using Eq. (5) (black lines) is applied to the delayed EL after the pulse end for $\tau = 0.5$–50 μs. The delayed EL and fits to Eq.(5) (lines) starting after the pulse end are plotted in a double logarithmic fashion in (c) for better illustration. In (d) time-resolved EL is presented from PLEDs driven with a fixed pulse length $\tau = 0.5$ μs and current densities $J = 0.2$ A/cm^2 (black diamond), 1 A/cm^2 (blue triangle), 10 A/cm^2 (red circle), and 30 A/cm^2 (green square). Additionally to the fit of Eq. (5) for t < 100 μs (black line), a power law with a slope of -1.3 is fitted to the delayed EL data for t > 100 μs (dashed line).

The reduction of delayed vs steady-state EL intensity with increasing current is a loss process for OLEDs and its origin is further discussed in Sec. V C.

C. Characterization of TA spectra from PLEDs

In order to reveal the origin of delayed EL and to gain quantitative insight into its decay dynamics, we performed TA measurements on working PLEDs. These measurements allow optical identification and quantification of excited states by their characteristic absorption features. The TA spectra are measured for a range of electrical drive pulse lengths of $\tau = 0.5$–50 μs and current densities $J = 0.2$–30 A/cm^2, the same conditions used for transient EL measurements. A representative electrical drive pulse with $\tau = 2$ μs at $J = 0.2$ A/cm^2 is shown in Fig. 6(a). During the first ~100 ns of the drive pulse, capacitive charging and ringing due to impedance mismatching is visible. However, 0.5 μs after the start of the drive pulse, the current pulse reaches its steady-state level [Fig. 6(a)].

The TA spectra during this drive pulse [Fig. 6(b)] were measured and averaged over the time slices of 0–50 ns (black line), 50–100 ns (green line), 0.75–1 μs (red line), and 1.5–2 μs (blue line) as represented by rectangles in Fig. 6(a). At all times a strong negative feature is visible in the TA spectra for $\lambda < 570$ nm [Fig. 6(b)]. This is electro-absorption (EA) of the ground state as a consequence of the Stark effect that is induced by the applied E-field.

At times $\leqslant$100 ns, a broad absorption band follows the EA band up to $\lambda \sim 800$ nm [Fig. 6(b)]. This is due to charge absorption around $\lambda = 550$–800 nm and is in agreement with TA measurements on F8BT hole-only devices [Fig. 6(c)]. As electrons and holes have very similar absorption spectra, the charge absorption measured in the bipolar device accounts for both charge carriers.[41] The charge absorption signal increases with increasing drive pulse duration [Fig. 6(b)] due to the buildup of space-charge zones and due to the accumulation of charges in the active layer. The presence of EA after the pulse end (not shown) is further evidence for the E-field of residual, long-lived charges in the emissive layer.

At times >100 ns, an additional transient absorption feature rises at $\lambda > 800$ nm as shown in the spectra averaged over 0.75–1 μs and 1.5–2 μs [Fig. 6(b)]. This is assigned to the triplet absorption, peaking at $\lambda \sim 800$ nm in agreement with optical (PIA) measurements.[28] The delayed rise of the triplet signal compared to the charge signal is caused by the duration for charges, mainly holes, to be transported through the F8BT layer until they reach the counterelectrode and recombine to triplets. Higher E-fields at higher current densities accelerate the transport of charges through the F8BT layer and reduce the delay of the triplet rise time. The absorption spectrum of triplets does not overlap with the charges for 810 nm $< \lambda <$

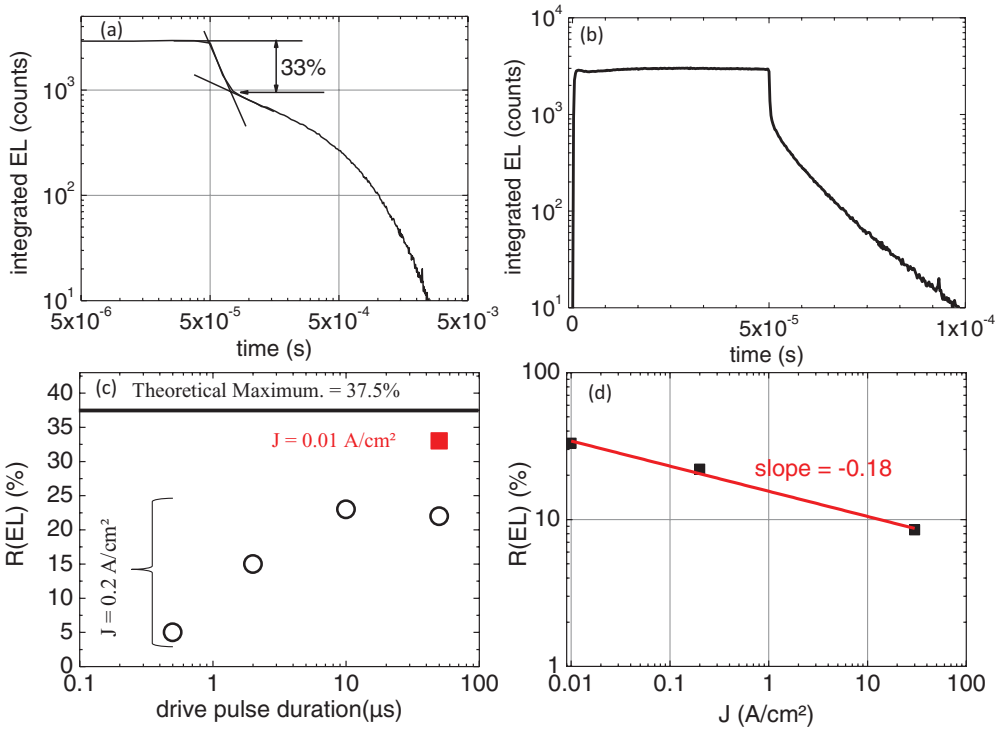

FIG. 5. (Color online) (a) Time-resolved EL intensity for a 50 μs electrical pulse at 0.01 A/cm^2. The intensity of steady-state and delayed EL is identified by two horizontal lines, from which the contribution of delayed to steady-state EL intensity is measured to be 33%. The complete EL pulse is shown in a logarithmic-linear plot in (b). In (c) the contribution of delayed to steady-state EL intensity [R(EL)] is plotted for $J = 0.2$ A/cm^2 (open cicles) and for $J = 0.01$ A/cm^2 (filled, red square). R(EL) values are obtained from time-resolved EL measurements shown in Figs. 4(b) and 5(a). The theoretical maximum of R(EL) = 37.5% according to our model (Sec. III A) is shown as horizontal line. In (d) the fraction of saturated delayed vs steady-state EL intensity R(EL) (square) is plotted in a double logarithmic fashion vs the current density. A power law with the slope −0.18 (red line) is fitted to the data.

900 nm and is used in this range for calculations of the triplet density n_T as described in the Sec. III.

It is important to mention, that no stimulated emission or absorption feature of singlet states could be detected at any current density. This can be explained by the low singlet density due to their short lifetime, resulting in signals orders of magnitude lower compared to triplet or charge signals.[42]

The derived triplet dynamics are presented for $J = 0.2$ A/cm^2 and a drive pulse length of $\tau = 0.5$–50 μs in Fig. 7 (symbols). The time required to reach the steady-state triplet density n_T^{SS} is ∼10 μs for $J = 0.2$ A/cm^2 [Fig. 7(a)]. The time for triplets to saturate is identical to the 10 μs rise time of prompt EL to reach steady-state intensity [Fig. 4(a)]. Furthermore the similarity of triplet [Fig. 7(b)] and delayed EL [Fig. 4(c)] decay dynamics indicates a connection between triplets and delay EL.

The device characteristics of studied PLEDs show high EQEs of 6.5% as described in Sec. IV A. This can be understood by a contribution of long-lived, delayed EL intensity after the pulse end to the steady-state EL intensity as characterized by transient EL measurements in Sec. IV B. TA measurements of excited states in the PLEDs are then described in Sec. IV C to gain a deeper insight into the processes that lead to delayed EL. The triplet and delayed EL decay dynamics are modeled in Sec. V A in order to identify and quantify the decay mechanism.

V. DISCUSSION

A. Triplet decay mechanisms

1. *Bimolecular triplet annihilation*

In order to characterize and understand the triplet decay and delayed EL mechanism in the PLEDs, the triplet decay model, described in Sec. III A is fitted to the experimental triplet decay dynamics. The validity of the triplet-triplet annihilation model for triplet decay processes in our PLEDs is supported by the excellent fit of Eq. (4b) to the experimental triplet dynamics (Fig. 7, symbols) after the pulse end. This provides evidence for triplet-triplet annihilation as the dominant decay process of triplets. Experimental data and fits after the end of the $J = 0.2$ A/cm^2 drive pulse are shown for better illustration and comparison in Fig. 7(b). The triplet-triplet annihilation rates at $J = 0.2$ A/cm^2 decrease from $\gamma_{TT}(\mathrm{TA}) = (1.6 \pm 0.2) \times 10^{-11}$ cm^3 s^{-1} to $(0.7 \pm 0.1) \times 10^{-11}$ cm^3 s^{-1} for increasing pulse length of $\tau = 0.5$ μs to $\tau \geqslant 10$ μs (Table I). A similar trend is found for the current dependence of γ_{TT}(TA). An increase in the current density from 0.2 to 30 A/cm^2 leads to a decrease of γ_{TT}(TA) from 1.6 to 0.7×10^{-11} cm^{3}s^{-1} (Table I). In both cases the decrease of γ_{TT}(TA) is due to the increase of the triplet densities n_T. Constant $\gamma_{TT}(\mathrm{TA}) = (0.7 \pm 0.2) \times 10^{-11}$ cm^3 s^{-1} are found independent of pulse length and current density once triplet densities after the pulse end $T_0 \geqslant (3 \pm 1) \times 10^{16}$ cm^{-3} are reached (diagonal of Table I). This demonstrates nondispersive triplet transport that

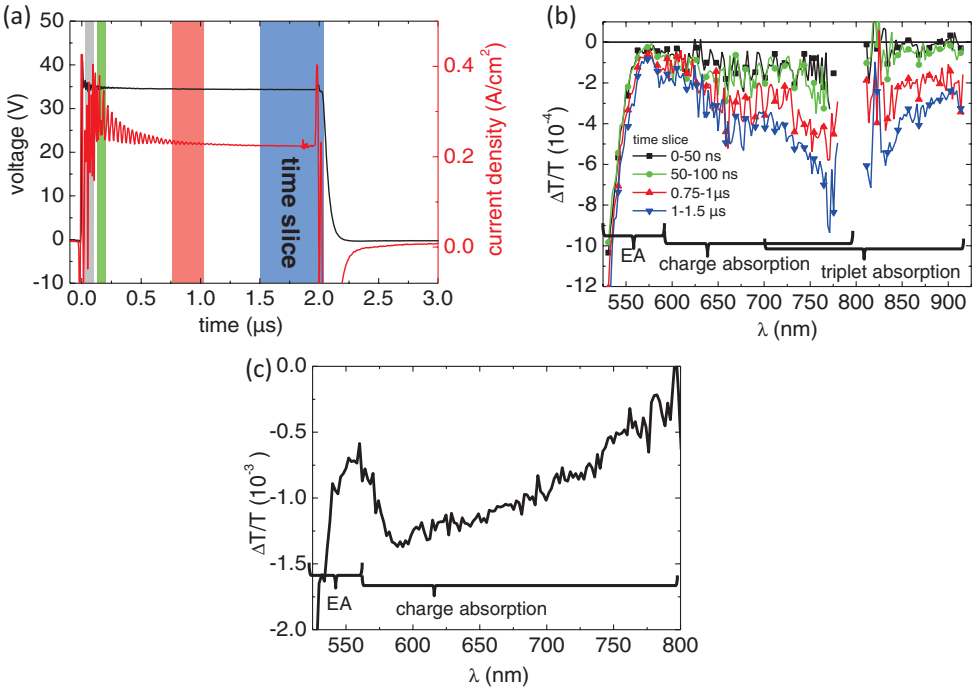

FIG. 6. (Color online) (a) Time-resolved current density (red line) and voltage (black line) characteristics of PLEDs driven with a 2-μs electrical pulse at 0.2 A/cm^2. Four key time slices are highlighted in grey (0–50 ns), green (50–100 ns), red (0.75–1 μs), and blue (1.5–2 μs) to identify the regions over which the TA spectra shown in (b) are averaged. (b) TA spectra averaged over the time slices shown in (a) are presented using the same color code. The brackets identify three dominant spectral signatures in the system, namely, electro-absorption (EA) for λ<560 nm, charge absorption for λ = 570–800 nm, and triplet absorption for λ = 700–950 nm. In (c) the TA spectrum of F8BT holes are shown. TA measurements were carried out at 10 A/cm^2 on the hole-only device glass/ITO (150 nm)/PEDOT (20 nm)/F8BT(300 nm)/MoO_3 (10 nm)/Au(100 nm), (PEDOT:PSS is poly(3,4-ethylenedioxythiophene) poly(styrenesulfonate)) where holes were injected through the MoO_3/Au electrode. The brackets identify the spectral region for EA (λ<560 nm) and hole absorption (λ = 560–800 nm).

is further supported by the excellent fit of the time independent triplet decay model [Eq. (4b)] to the triplet dynamics (Fig. 7).

Triplet-triplet annihilation rates for F8BT have been previously determined as $\gamma_{TT} = 1.72 \times 10^{-15}$ cm^{-3} s^{-1} by Ford *et al.* from CW-PIA measurements at low temperatures of 10 K.[28] The triplet transport changes from single-phonon-assisted tunneling at temperatures below 50 to 100 K to thermally activated multiphonon hopping at room temperature where our experiments are carried out.[43] This increases the triplet transfer rate by three to four orders of magnitude and thus increases the triplet-triplet annihilation rate to 0.7×10^{-11} cm^{-3} s^{-1}.[43] The presented value is in agreement with a very similar value of $\gamma_{TT} = 0.4 \times 10^{-11}$ cm^{-3} s^{-1}, determined for F8BT from TA measurements using optical excitation.[44] Lower triplet-triplet annihilation rates of 1.4×10^{-14} cm^3 s^{-1} have been reported for small molecules

TABLE I. F8BT triplet-triplet annihilation rates γ_{TT} from the fit of Eqs. (4b) and (5) applied to the TA and time-resolved EL measurements (grey) for J = 0.2–30 A/cm^2 and pulse length τ = 0.5–50 μs. Additionally, F8BT monomolecular decay rates $k_T(n_c)$ are listed. They are determined from the fit of Eq. (5) to the time-resolved EL measurements shown in Figs. 4(b)–4(d).

	τ	0.5 μs		2 μs		10 μs		50 μs	
Type	J (A/cm^2)	γ_{TT} (10^{-11} cm^3 s^{-1})	$k_T(n_c)$ (10^{-4} s^{-1})	γ_{TT} (10^{-11} cm^3 s^{-1})	$k_T(n_c)$ (10^{-4} s^{-1})	γ_{TT} (10^{-11} cm^3 s^{-1})	$k_T(n_c)$ (10^{-4} s^{-1})	γ_{TT} (10^{-11} cm^3 s^{-1})	$k_T(n_c)$ (10^{-4} s^{-1})
TA	0.2	1.6 ± 0.2	–	1.3 ± 0.1	–	0.7 ± 0.1	–	0.7 ± 0.1	–
EL	0.2	2.0 ± 0.2	2.7 ± 0.1	1.1 ± 0.1	2.8 ± 0.1	0.6 ± 0.1	2.9 ± 0.1	0.7 ± 0.1	3.1 ± 0.3
TA	1	1.2 ± 0.1	–	0.9 ± 0.1	–	0.7 ± 0.1	–	–	–
EL	1	1.4 ± 0.1	3.3 ± 0.1	–	–	–		–	–
TA	5	0.9 ± 0.1	–	0.7 ± 0.1	–		–	–	–
EL	5	–	–	–	–	–	–	–	–
TA	10	0.8 ± 0.1	–	0.6 ± 0.1	–		–	–	–
EL	10	0.8 ± 0.1	3.7 ± 0.1	–	–	–		–	–
TA	30	0.8 ± 0.1	–	–	–	–	–	–	–
EL	30	0.7 ± 0.2	4.1 ± 0.1	–	–	–	–	–	–

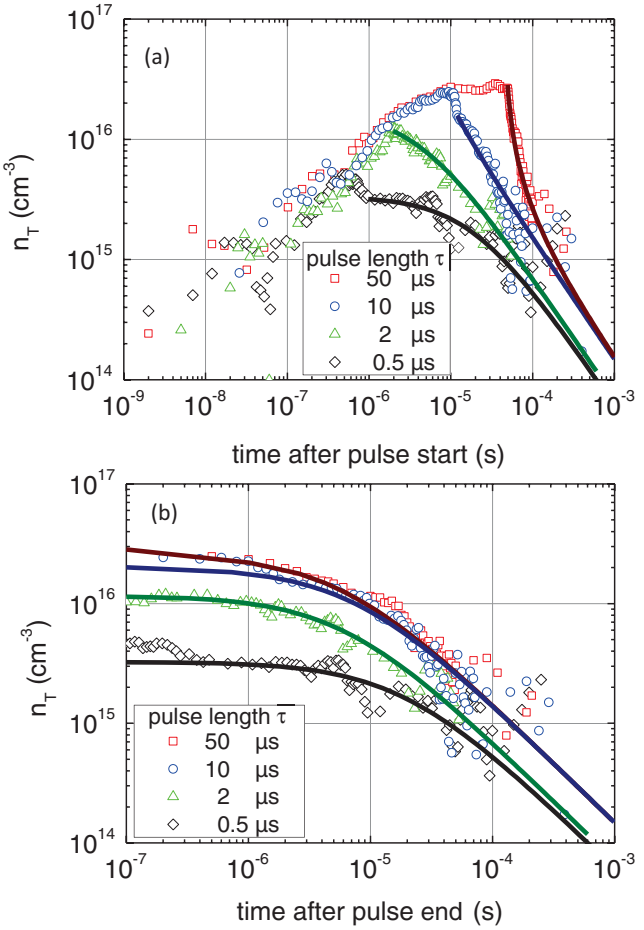

FIG. 7. (Color online) Double logarithmic presentation of triplet densities n_T (symbols) measured via transient absorption spectroscopy in PLEDs driven at $J = 0.2$ A/cm^2 for pulse length $\tau = 0.5\ \mu$s (black diamond), 2 μs (green triangle), 10 μs (blue circle), and 50 μs (red square). The triplet decay model presented in Eq. (4b) is fitted to the experimentally measured triplet densities after the pulse end and presented as plain lines using the same color code as the symbols. The extracted bimolecular annihilation rates are presented in Table I. For better illustration of the triplet decay dynamics and comparison of different drive pulse length, triplet densities and fits starting after the end of each pulse are shown in (b).

such as 4,4′-bis(carbazol-9-yl)1,1′-biphenyl (CBP).[45] The difference to our values can be explained by the difference in triplet transport for polymers and small molecules. Triplet transport, which occurs via Dexter energy transfer, is significantly accelerated and more efficient in polymers compared to small molecules.[43] This has been explained by a lower activation energy for hopping because of lower geometric distortion as a consequence of larger wave function delocalizations on polymer chains compared to small molecules. Furthermore, the wave function overlap between the initial and final site significantly increases for polymers compared to small molecules, leading to accelerated triplet diffucion and bimolecular annihilation.[43] Triplet diffusion and thus triplet-triplet annihilation is further accelerated by aggregation and allignment of polymer chains. These morphologies are present in spin-coated polymer films,[46] as used here.

Characterization of bimolecular annihilation as the main triplet decay process points toward emissive singlet states generated from triplet-triplet annihilation as the origin of delayed EL after the pulse end (Sec. IV B). If nonemissive triplet states are responsible for delayed EL, we can apply the triplet decay model [Eq. (5)] to the delayed EL dynamics to model triplet decay mechanisms. In order to derive absolute triplet decay rates from the model, we use the triplet density at the pulse end T_0 from TA measurements. The excellent fit of the model [Eq. (5)] to the delayed EL data is displayed in Figs. 4(b)–4(d). It provides further evidence for triplet-triplet annihilation as the dominant triplet decay mechanism and for singlets generated from triplet-triplet annihilation as the origin of delayed EL. The derived rates, γ_{TT}(EL) are virtually identical to the γ_{TT}(TA) values modeled from TA measurements, as summarized in combination with the derived monomolecular triplet decay rates $k_T(n_c)$ in Table I.

From the derived γ_{TT} values, we are able to estimate the triplet diffusion coefficient $D_T = \frac{\gamma_{TT}}{8\pi\langle R\rangle}$, assuming an average reaction distance between two triplets as a constant value described in literature by $\langle R\rangle \sim 0.5$ nm.[5] The calculated value $D_T = (9 \pm 4) \times 10^{-6}$ cm^2/s for F8BT in our PLEDs is comparable with $D_T = (1.7 \pm 0.2) \times 10^{-6}$ cm^2/s for PhLPPP.[47] We use this diffusion coefficient to give an estimation of the triplet diffusion length, described by $L = \sqrt{D\langle\tau\rangle}$.[47] Therefore, we determine the average triplet lifetime $\langle\tau\rangle$ as the time when the triplet density is reduced to $1/e$ of its maximum value T_0. This provides a decreasing diffusion length $L = (178$–$30)$ nm for increasing current of $J = 0.2$–30 A/cm^2. The increase of current density leads to (i) an increase of the triplet density and thus accelerated triplet-triplet annihilation and (ii) an increase of the charge density and thus accelerated triplet-charge annihilation. These effects result in a decrease of the average triplet lifetime $\langle\tau\rangle$. The diffusion length for triplets in the studied F8BT PLED is similar to triplet diffusion length of 140 nm for Alq_3.[48]

In order to understand the steady-state behavior of PLEDs, we determine steady-state triplet density n_T^{SS} and the time to reach steady-state conditions t_{ss} from the triplet dynamics at $J = 0.2$–30 A/cm^2.

We find the dependence of n_T^{ss} on J to follow a power law, where $n_T^{ss} \propto J^{\frac{1}{3}}$ [Fig. 8(a)]. The exponent $1/3$ is lower than the expected value of $1/2$, which is derived from the steady-state solution of the triplet rate equation [Appendix, Eq. (A1)], given as $n_T^{ss} = (\frac{G}{\gamma_{TT}})^{0.5}$ and leading to $n_T^{ss} \propto J^{\frac{1}{2}}$ assuming that $G \propto J$. The low slope of the triplet steady-state density vs current density points toward loss processes for triplets with increasing current density. These loss processes as well as the dependency $t_{ss} \propto J^{-0.5}$ [Fig. 8(b)] are addressed by complementary measurements in Sec. V C.

We can assign the origin of delayed EL to singlets generated from triplet-triplet annihilation. Besides triplet-triplet annihilation, we revealed an additional origin of delayed EL. We found a significant change in the delayed EL dynamics for $t > 100\ \mu$s after the start of the pulse [Fig. 4(d)] when the experimental data deviates from the fit of Eq. (5) and decays as $\propto t^{-1.3\pm0.1}$ [Fig. 4(d), dashed line]. This strong reduction of delayed EL intensity is due to a strong depletion of triplet density as the consequence of strong triplet-triplet

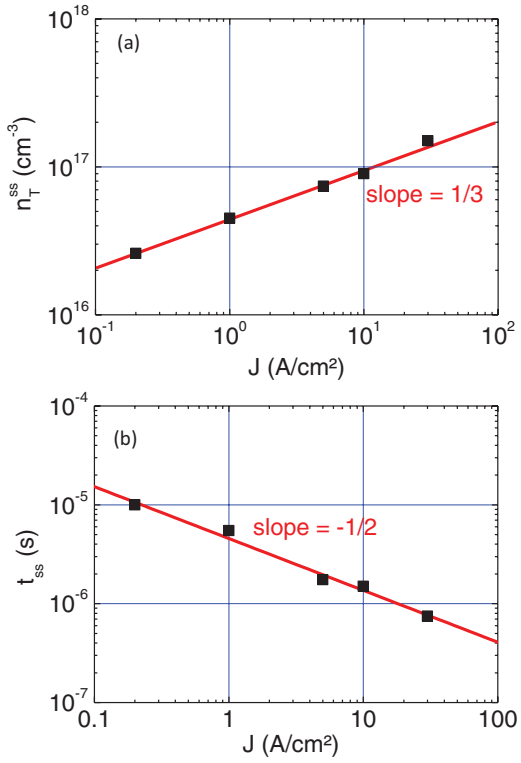

FIG. 8. (Color online) (a) Steady-state triplet density n_T^{SS} (black squares), derived from TA measurement (i.e., Fig. 7(a) for $J = 0.2$ A/cm^2) vs current density J in a double logarithmic plot. In (b) the time t_{ss} to reach steady-state density n_T^{SS} is plotted vs the current density J. Power laws with slopes 1/3 (a) and $-1/2$ (b) are shown as red lines.

annihilation. The residual, weak, delayed EL is assigned to recombination of charges removed from shallow traps. The EL intensity generated from charge recombination dominates the delayed EL for $t > 100$ μs. Evidence for the recombination of charges from intrinsic, shallow traps is the virtually identical intensity and slope of delayed EL over more than one order of magnitude of current density $J = 0.2$–30 A/cm^2 [Fig. 4(d)].

2. *Monomolecular triplet decay*

The sensitivity of time-resolved EL measurements is significant higher compared to TA measurements. This gives further insight into triplet decay processes at low triplet densities ($\ll 10^{15}$ cm^{-3}). It is sensitive enough to determine monomolecular triplet decay rates $k_T(n_c)$ from the fit of Eq. (5) to delayed EL measurements. The $k_T(n_c)$ values increase from 2.7 to 4.1×10^4 s^{-1} (Table I) with increasing current density from 0.2 to 30 A/cm^2 [Fig. 4(d) and Table I]. The increase of the monomolecular triplet decay with voltage points to charge-induced triplet losses and will be discussed in Sec. V C. This current-induced increase of $k_T(n_c)$ is in agreement with a slight increase of $k_T(n_c) = 2.7$–3.1×10^4 s^{-1} as the charge density slightly increases with pulse length $\tau = 0.5$–50 μs [Fig. 4(b) and Table I].

By extrapolating the $k_T(n_c)$ values to a current and voltage free case, we calculate the unperturbed triplet lifetime $\tau_{T,0} = 43$ μs at 300 K. Previously, Dhoot *et al.* have determined $\tau_{T,0} = 571$ μs at 12 K by CW-PIA.[27] The difference in our values measured at room temperature can be explained by the thermally activated triplet transport.[43]

We identified triplet-triplet annihilation as the dominant triplet decay mechanism from the triplet as well as delayed EL dynamics and reveal singlets generated by triplet-triplet annihilation as the origin of delayed EL. From our triplet decay model, we derive bimolecular and monomolecular triplet decay rates.

B. Contribution of triplet-triplet annihilation to the device efficiency

The large fraction of delayed compared to steady-state EL intensity (Sec. IV B) demonstrates a strong contribution of singlets generated from triplet-triplet annihilation to the steady-state singlet density. The contribution of delayed to steady-state EL intensity is 22% for $J = 0.2$ A/cm^2 [Fig. 5(c)] in agreement with the ~20% rise of the prompt EL intensity during the pulse between 0.5–10 μs [Fig. 4(a)]. The rise time of 10 μs is identical to the saturation time for the delayed EL intensity [Fig. 4(c)] and for triplets [Fig. 7(a)], providing further evidence for triplet-triplet annihilation as the origin of the delayed EL. By reducing the drive current to 10 mA/cm^2, we reach a maximum contribution of 33% from triplet-triplet annihilation to steady-state brightness and efficiency, which is close to the theoretical maximum of 37.5% [Fig. 5(c)].

The experimental finding of 33% delayed to steady-state EL supports our triplet decay model described in Sec. III A and Fig. 2. Two important conclusions emerge:

(i) For the PLEDs studied here, effectively all triplets are available for triplet-triplet to singlet generation. Given that we expect triplet generation to be near to the cathode, closer than the triplet excitons diffusion range, the ZnO cathode used here must function as a loss-less "reflector" of excitons back into the bulk. The selection of cathodes with this property is therefore necessary for efficient device operation.

(ii) Multiple passes through the triplet-triplet annihilation cycle are mandatory in order to reach the experimentally confirmed contributions of 33% singlets generated by triplet-triplet annihilation to the overall singlet density and to reach the theoretical maximum contribution of 37.5% (Sec. III A). Triplet-triplet annihilation leads to a maximum of additional 15% singlets (Eq. 2). These singlets have to be added to 25% singlets generated from charge recombination to yield the total fraction of 40% singlets. It is important to emphasize that these high singlet amounts can be realized without violating spin statistics. The contributions of singlets generated from triplet-triplet annihilation have to be carefully considered for experimental determination of singlet-to-triplet ratios. Our theoretical maximum for the singlet generation of 40% without violating spin statistics is comparable to the singlet yield of 44 ± 4% recently determined for polyfluorenes[16] and of 40 ± 5% reported for poly(para-phenylene vinylene) (PPV).[49]

We have presented a model in which singlets generated from triplet-triplet annihilation can form up to 37.5% of the total singlet density by measuring the contribution of delayed to steady-state EL intensity. In order to understand the contributions of triplet-triplet annihilation to the EQE [Fig. 3(b)] in our PLEDs, we compare the EQE and the contribution of delayed to steady-state EL intensity depending

on current density. EQE of these devices gradually rises at lower current densities and saturate at 6.5% EQE for $\sim$100 mA/cm^2 [Fig. 3(b)].

Singlets generated from triplet-triplet annihilation contribute up to 33% to the device EQE at current densities of 10 mA/cm^2, what is significantly below the current density at the EQE maximum (100 mA/cm^2). The contribution of triplet-triplet annihilation to the device efficiency decreases with increasing current. Its contribution is reduced to $\sim$22% for J $\sim$100 mA/cm^2 at the EQE maximum [Fig. 5(d)]. Further increase of the current density leads to the efficiency roll-off, as described by Kabra *et al.*[9] in more detail.

From the transient EL measurements, we identify a contribution of 22% from triplet-triplet annihilation to the steady-state device efficiency at the EQE maximum. This is one important explanation for high EQEs of 6.5% in these devices. For a comprehensive picture, it is important to consider other reasons that could explain the high EQE. A deviation of the singlet generation rate from 25% would strongly affect the EQE of fluorescent devices. The determination of absolute singlet generation rates is extremely challenging and not possible with the presented results. Various approaches using a combination of optical and electrical or optical and magnetic resonance techniques have been used for experimental determination of η_{spin} leading to a broad range of singlet vs triplet generation fractions from 15–94%.[16,27,33,34,50–52]

The EQE is furthermore affected by the coupling of light out of the device into free space. It is experimentally challenging and beyond the focus of this paper to determine the outcoupling factor and its dependency on device parameters. Detailed investigations have shown that preferred orientation of emissive dipoles in the film plane can reduce the coupling of emitter dipoles to lossy surface plasmon modes and thus increase the EQE due to improved coupling of light into free space.[53] Preferential orientation of polymer chains in the film plane[46] and the introduction of high refractive index ZnO and MoO_3 layers might improve the coupling of light out of our PLEDs into free space and contribute to its high EQE.[11]

C. Study of the current-dependent decrease of the delayed to steady-state EL intensity ratio

In this section, we investigate triplet loss processes, which reduce the delayed to steady-state EL intensity from 33% at 0.01 A/cm^2 to 8.5% at 30 A/cm^2 [Fig. 5(d)].

1. *Characterization of triplet-charge annihilation*

The monomolecular triplet decay rates $k_T(n_c)$ have been determined from the delayed EL dynamics as described in Sec. V A and are presented in Table I. The increase of $k_T(n_c)$ with current density is expected to originate from increasing triplet-charge annihilation caused by rising charge density.

In order to calculate the triplet-charge annihilation rate γ_{TC}, the density of charge that can interact with a triplet is required. Charge densities are estimated for the volume where interaction of both can take place. According to our model (Sec. III B), the space-charge zone of dominant holes reaches from the anode up to the recombination zone, which is located close to the cathode. By assuming a triplet diffusion length of (105 ± 75) nm from the cathode toward the anode, triplets can interact with the fraction $\theta = (0.7 \pm 0.2)$ of the mean hole density $\langle n_c \rangle$ in the device, as described by Eq. (9) in Sec. III B.

The $k_T(n_c)$ values (Table I) were measured 70 ± 20 μs after the pulse end, when the charge density is reduced compared to its steady-state value. The ratio of the charge density at times 70 ± 20 μs after the pulse compared to its steady-state density can be estimated approximately from the comparison of the charge absorption at both times. The charge absorption during the pulse at 600 nm $\leqslant \lambda \leqslant$ 700 nm is shown in Fig. 6(b). At 70 ± 20 μs after the pulse, the charge absorption and thus the charge density is 20 ± 10 times smaller compared to the steady-state density (not shown). Residual charges in the device cause electro-absorption (EA) of the ground state for $\lambda \leqslant 560$ nm after the pulse end (not shown). The EA at 70 ± 20 μs after the pulse compared to the steady-state EA is reduced by the same factor as the charge absorption. From these charge densities, we are able to approximately estimate the triplet-charge annihilation rate $\gamma_{TC} = (1.3 \pm 1.0) \times 10^{-11}$cm^3 s^{-1} from the plot of the relative change of the monomolecular triplet decay rate $(\Delta k/k_0)$ vs voltage [Fig. 9(a)] according to [Eq. (10)]. Even though we find a good fit of the model [Eq. (10)] to the data [Fig. 9(a)], the charge distribution after the pulse end is likely to differ from the distribution of the steady-state space-charge zone. The resulting change in charge density would then affect the γ_{TC} value (Sec. III B). Hence, we have to consider $\gamma_{TC} = (1.3 \pm 1.0) \times 10^{-11}$ cm^3 s^{-1} as a qualitative estimate.

Triplet-charge annihilation rates have been determined previously to $(4 \pm 1) \times 10^{-13}$ cm^3 s^{-1} for a 2,3,7,8,12,13,17,18-octaethylporphine platinum (PtOEP)-doped polyfluorene system[54] and to $(2–7) \times 10^{-13}$ cm^3 s^{-1} for phosphorescent, small molecule guest host systems.[55] We consider that the larger value we find for the polymer system arises from the high triplet exciton diffusion coefficient, as estimated for triplet-triplet annihilation as mentioned in Sec. V A.[54,55]

Nonpolar triplets are not attracted by the columbic field of charges, and thus both are expected to annihilate in a diffusion-limited reaction. We calculate the average reaction distance $\langle R_{TC} \rangle$ between a triplet and a charge according to Smoluchowski's equation $\langle R_{TC} \rangle = \frac{\gamma_{TC}}{4\pi(D_T + D_C)}$, where D_c is the diffusion coefficient of the charge. As holes are the dominant charges, the diffusion coefficient D_h for holes is used in first approximation as the charge diffusion coefficient. It is calculated via Einstein relation[40] $D_h = \frac{\mu k_B T}{q}$, where k_B is the Boltzmann constant, T is the temperature, and q is the electrical charge. By assuming a field-dependent mobility of $\mu = \mu_0 e^{(\beta\sqrt{\frac{V}{d}})} = 10^{-4}$ cm^2/Vs at 30 V as described in Sec. III B, we derive $D_h = 3 \times 10^{-6}$ cm^2/s. With $D_T = (9 \pm 4) \times 10^{-6}$ cm^2/s the estimated average reaction distance for triplet-charge annihilation is derived in first approximation as $\langle R_{TC} \rangle = (1.5 \pm 1.2)$ nm. This value is slightly higher compared to the average reaction distance for triplet-triplet annihilation of $\sim$0.5 nm as found in literature.[5] The difference can be explained by the different size of both species. The charge causes a polarization of its close environment that leads to a spatially extended polaron, in contrast to the more localized, nonpolarized triplet. Calculations have shown that polarons can extend over 20 C atoms,[56] which is the

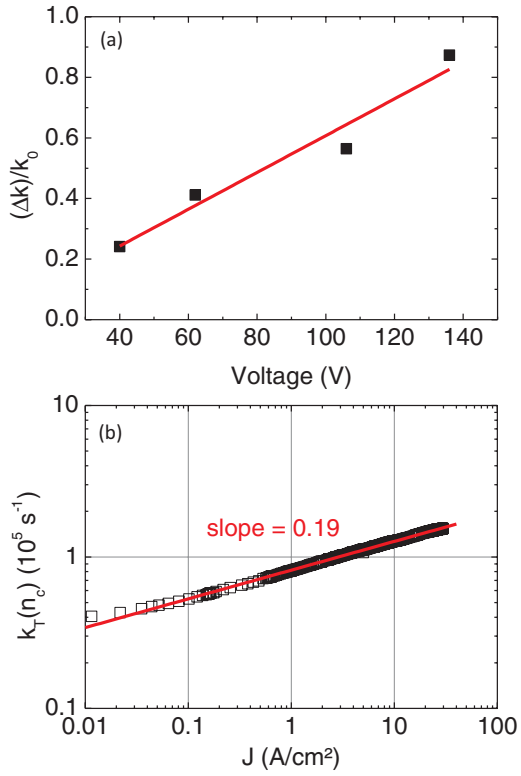

FIG. 9. (Color online) (a) The relative change of the monomolecular triplet decay (square) is plotted against the drive voltage of the PLED. The triplet-charge annihilation rate $\gamma_{TC} = (1.3 \pm 1.0) \times 10^{-11}$ cm^{3}s^{-1} is determined from the fit of Eq. (10) (line) to the data. Calculated triplet decay rates $k_T(n_c)$ during the electrical drive pulse (open square) are plotted in (b) vs current density in order to describe triplet losses by triplet-charge annihilation. The triplet decay rates $k_T(n_c)$ during the electrical pulse are calculated according to Eq. (8). The charge density during the pulse is estimated by applying the SCLC model, Eq. (9), to the experimental *J-V* characteristics that are shown is Fig 3(c). The k_T vs J characteristics are fitted to a power law with the slope 0.19, as shown by a red line.

range of the estimated $\langle R_{TC} \rangle$ value. Hence, the triplet-charge interaction may take place over a larger interaction range compared to triplet-triplet interaction and is a significant loss channel for triplets. The slightly higher reaction distance for triplet-charge annihilation compared to the value for triplet-triplet annihilation further supports the validity of our rather high triplet-charge annihilation rate.

Triplet losses by triplet-charge annihilation are significantly higher during the pulse than when the monomolecular decay is measured (70 ± 20 μs after the pulse end), as the charge carrier density is 10–30 times higher. Furthermore, the amount of triplets lost by triplet-charge annihilation increases significantly with drive voltage as the charge density increases proportionally [Eq. (9)]. We estimate the triplet losses by triplet-charge annihilation during the pulse by calculating the $k_T(n_c)$ value according to Eq. (8). The charge density during the pulse is estimated by applying the SCLC model, Eq. (9), to the experimental *J-V* characteristics that are shown is Fig 3(c). The estimated $k_T(n_c)$ values, and thus triplet losses by triplet-charge annihilation, show a dependency on the current density of $k_T(n_c) \propto J^{0.19}$ as illustrated in Fig. 9(b). The increase of $k_T(n_c)$ results in an increase of triplet losses and in a decrease of the steady-state triplet density n_T^{ss} with increasing current density. Experimental results show that the current dependency follows a power law of $n_T^{ss} \propto J^{1/3}$[Fig. 8(a)]. The exponent of 1/3 is lower than the theoretically expected value of 1/2 that we derive from the steady-state solution of the triplet rate equation, where $n_T^{ss} \propto J^{1/2}$ assuming that $G \propto J$ (Sec. V A). The increase of triplet losses, described by $k_T(n_c) \propto J^{0.19}$, accounts for the deviation of the experimental steady-state triplet density ($\propto J^{1/3}$) from theory ($\propto J^{1/2}$).The reduction of n_T^{ss}, then, results in a decrease of the delayed vs steady-state EL intensity ratio R(EL), as triplets account for 100% of delayed EL intensity but only 8.5–33% of steady-state EL intensity. The decrease of R(EL) vs J is described by $R(\mathrm{EL}) \propto J^{-0.18}$ as shown in Fig. 5(d). The correlation between the decrease of R(EL) ($\propto J^{-0.18}$) and the increase of $k_T(n_c)$ ($\propto J^{0.19}$) is a further indication for triplet-charge annihilation as the origin of triplet losses, the reduction of n_T^{ss} and thus R(EL). It is noteworthy that these explanations do not require absolute γ_{TC} values as they are based on the current-dependent change of $k_T(n_c)$.

2. *Characterization of the triplet generation processes*

In order to understand the reduced delayed vs steady-state EL intensity at high current densities, we investigate the current dependency of the triplet generation rate and compare it to the emissive rate for prompt EL.

The model, used to derive the triplet generation rate G_0 and the width of the recombination zone $1/\lambda$ is described in detail in the Appendix. From the current density dependency of the generation model (Appendix), we derive the saturation time for triplets, $t_{\mathrm{SAT}} \propto (G_0 \lambda \gamma_{TT})^{-0.5}$. For $G_0 \lambda \propto J$ and constant γ_{TT}, we derive the dependency $t_{ss} \propto J^{-0.5}$, which is in agreement with experimental finding shown in Fig. 8(b). Furthermore, it establishes the validity of the triplet generation model and its connection to the triplet decay model (Sec. III A).

The fits of this model to the experimental data are shown in Fig. 10 and the derived values for G_0 and $1/\lambda$ are displayed in Table II. The current dependency of the width of the recombination zone $1/\lambda$ is further discussed in the appendix.

From the current dependency of G_0, we find the relation $G_0 \propto J^{0.82}$ (Fig. 11, solid blue line) that is in contrast to the general assumption of the linear relation $G_0 \propto$J. In order to describe a dependency of the steady-state triplet density n_T^{ss} on the current density, we derived the relation $n_T^{ss} \propto G_0^{\frac{1}{2}}$ from the steady-state solution of the triplet rate equation (Sec. V A). By combining it with our experimental finding $G_0 \propto J^{0.82}$, we derive approximately the dependency $n_T^{ss} \propto J^{1/3}$ that we found experimentally, as shown in Fig. 8(a). The triplet generation rate G_0 describes the slope of the rising triplet density at early times (Fig. 10). This is obvious as the model can be simplified at early times to $a_T(t \rightarrow 0) = G_0 t$. Hence, the reduction of G_0 with increasing current density must be due to triplet losses at times up to 10 μs at 0.2 A/cm^2 and 1 μs at 30 A/cm^2. Triplets are more strongly affected by charges than singlets, as they are longer lived. This results in enhanced triplet losses by annihilation with charges (Sec. V C 1). These losses reduce not only n_T^{ss} during the whole pulse length but reduce also G_0 at early

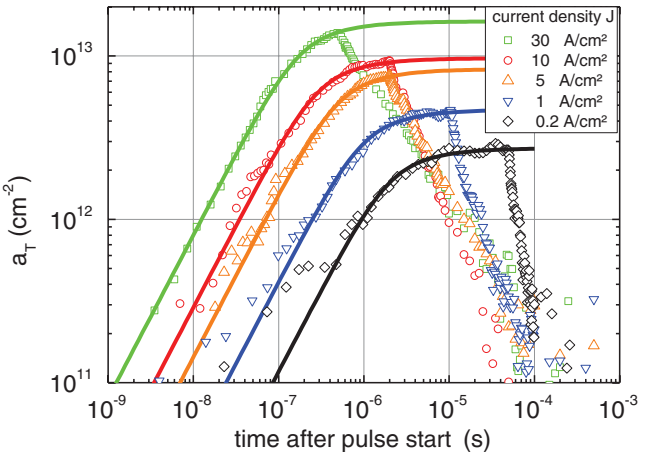

FIG. 10. (Color online) Plot of the triplet area densities a_T, determined via TA spectroscopy for $J = 0.2$ A/cm^2 (black circle), 1 A/cm^2 (blue triangle, top down), 5 A/cm^2 (orange triangle, top up), 10 A/cm^2 (red circle), and 30 A/cm^2 (green square). The triplet model (Appendix) is fitted to the experimental data and plotted (lines) using the same color code. From these fits, the generation rate G_0 and the width of the recombination zone $1/\lambda$ are obtained and presented in Table II.

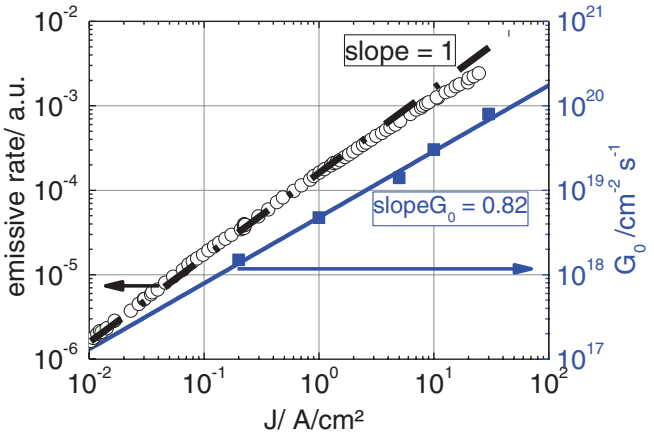

FIG. 11. (Color online) Double logarithmic presentation of the triplet generation rate G_0 (blue squares), derived from the triplet generation model (Appendix and Table II), and the emissive rate (black circles), derived from pulsed brightness measurements ($\tau = 10\ \mu$s) plotted vs the current density J. The exponent of the power-law of the triplet generation rates (blue squares) is determined to be 0.82 (blue line) over the $J = 0.2$–30 A/cm^2 range. A black, dashed line with the slope 1 is shown as a guide for the eye to compare the slope of the emissive rate with the slope of G_0.

times of the pulse. This contributes to the reduction of delayed vs steady-state EL intensity as discussed in Sec. V C 1.

In order to compare the current dependency of G_0 and thus the delayed EL intensity with the prompt EL intensity, we determined the prompt emissive rate from pulsed current density-voltage-luminance (*J-V-L*) measurements with $\tau = 10$ μs [Fig. 10, (circles)] The prompt emissive rate rises linearly ($\propto J^1$) for the range of $J = 0.01$–1 A/cm^2 (Fig. 11 dashed, black line). This proportionality to the current is expected. A weak decrease of the prompt emissive rate leads to a slightly sublinear slope for $J > 2$ A/cm^2 (Fig. 11) due to increasing loss processes of singlets.[9] By comparing the current dependency of G_0 and the prompt emissive rate, we find a divergence of both slopes, shown in Fig. 11. The difference between the slope of the emissive rate ($\propto J^1$) and G_0 ($\propto J^{0.82}$) is in agreement with the current-dependent increase of $k_T(n_c)$ ($\propto J^{0.19}$) and points toward triplet-charge annihilation as the origin of reduced G_0 values and the reduced ratio of delayed vs steady-state EL intensity.

The excellent fits of the triplet generation and decay models to the experimental transient absorption and transient EL data provides evidence for the validity of these models and the applicability to experimental data from our PLEDs.

TABLE II. Generation rate G_0 and the width of the triplet recombination zone $1/\lambda$ for current densities of $J = 0.2$–30 A/cm^2, derived from Fig. 10 using the triplet generation model (Appendix).

J (A/cm^2)	G_0 (cm^{-2} s^{-1})	$1/\lambda$ (nm)
0.2	1.2×10^{18}	127
1	4.2×10^{18}	107
5	1.4×10^{19}	97
10	2.9×10^{19}	65
30	8.0×10^{19}	66

VI. CONCLUSION

We have studied the effect of triplet dynamics in fluorescent PLEDs in order to explain the high efficiencies of these devices. We introduced a novel TA technique and combined it with time-resolved EL measurements for detailed, quantitative investigations of the triplet decay processes in working, fluorescent PLEDs. We characterized triplet-triplet annihilation as the dominant triplet decay mechanism and determined bimolecular triplet-triplet annihilation rates $\gamma_{TT} = (0.7$–$2) \times 10^{-11}$ cm^3 s^{-1} and monomolecular decay rates $k_T(n_c)$ in the range 2.7–4.1 $\times 10^4$ s^{-1} from a triplet decay model.

Singlet states generated by triplet-triplet annihilation cause strong, delayed EL after the pulse end that contributes up to ~33% to steady-state device brightness and efficiency. The experimental results are in agreement with our triplet model, which assumes that triplet states undergo triplet-triplet annihilation several times. We demonstrate that the total amount of singlets generated from triplet-triplet annihilation, together with singlets generated from charge recombination, can reach a theoretical maximum of 40% of all excitons formed by charge recombination without violating the spin statistic model.

The large contribution of delayed to steady-state EL intensity decreases significantly with increasing current densities and is reduced to 22% at the current densities of the maximum external quantum efficiency. This reduction of delayed to steady-state EL intensity is due to increased triplet-charge annihilation with increasing current density at an estimated rate of $(1.3 \pm 1.0) \times 10^{-11}$ cm^3 s^{-1}. Current-dependent triplet losses are confirmed by the current-dependent decrease of the determined triplet generation rate. With these investigations we give a comprehensive, quantitative picture of triplet generation and decay processes, delay EL dynamics and their contribution

to the singlet fraction, and thus efficiency in fluorescent PLEDs, which has not been carried out before.

ACKNOWLEDGMENTS

The authors are thankful to Cambridge Display Technology for supply of F8BT as well as to the Engineering and Physical Sciences Research Council (UK) for financial support through the Basic Technology Research Grant Initiative COSMOS (Coherent Optical Sources using Micromolecular Ordered Structures), EP/D0489X/1. B. H. Wallikewitz is thankful to A. S. Dhoot for fruitful discussions.

APPENDIX: GENERATION AND DECAY PROCESSES DURING THE PULSE

For the investigation of processes during the electrical drive pulse, the generation of triplets from charge recombination is modeled by adding a generation rate G to the triplet decay model Eq. (4a). As described by Rothe *et al.*,[14,16] this can be done by assuming a constant generation rate G throughout the whole active layer using rate Eq. (A1) with the analytical solution Eq. (A2):

$$\frac{dT(t)}{dt} = G - \gamma_{TT}[T(t)]^2, \tag{A1}$$

$$[T] = \frac{G}{\gamma_{TT}} \tanh(t\sqrt{G\gamma_{TT}}). \tag{A2}$$

Unfortunately, this model gives a poor fit to the experimental data, resulting in an incorrect calculation of the steady-state triplet density.[14,16] In agreement with Rothe *et al.*, we find that a better agreement is obtained by assuming an exponential decay of the triplet generation rate G_0 from the ZnO cathode in x direction toward the anode.[14,16] This assumption is valid for our PLEDs, as the device is hole dominated due to their higher mobility than that of electrons, resulting in charge recombination and exciton formation close to the cathode. The density of generated triplets decays exponentially in the F8BT layer toward the anode.[9] This is represented as Eq. (A3). It has to be integrated over the film thickness (x direction) because we are interested in the total generation rate. Its analytical solution is then given by Eq. (A4)

$$\frac{dT(x,t)}{dtdx} = G_0\lambda e^{-\lambda x} - \gamma_{TT}[T(x,t)]^2, \tag{A3}$$

$$a_T = \frac{2}{\lambda\gamma_{TT}t} \ln[\cosh(t\sqrt{G_0\lambda\gamma_{TT}})]. \tag{A4}$$

It is important to mention that a_T is the density of triplets per area and not per volume as used in Eq. (A2). This is a consequence of the integration over the film thickness. It is also important to consider that G_0 is given in the units $\mathrm{cm}^{-2}\mathrm{s}^{-1}$ and λ is the reciprocal length of the recombination zone at $1/e$ of its initial value.

The fits of the model to the experimental data are shown in Fig. 10, and the derived values for G_0 and $1/\lambda$ are displayed in Table II. The width of the triplet recombination zone $1/\lambda$, reaches 127 nm at the lowest current density of 0.2 $\mathrm{A/cm}^2$ (Table II). This is more than one order of magnitude larger compared to values reported for devices with polyspirobifluorene polymers as active materials.[14] Our results confirm previous assumptions of a broad recombination zone as one explanation of the high efficiency of these PLEDs[9]. A broad recombination zone is advantageous as it reduces loss processes of singlets like singlet-charge and singlet-triplet annihilation. A broad recombination zone compared to a narrow one is also advantageous for triplet-triplet annihilation, as less triplet states diffuse out of the recombination zone and are lost by triplet-charge annihilation. For increasing current densities $\geqslant$10 $\mathrm{A/cm}^2$, we find a decrease of the recombination zone width to 65 nm (Table III). Narrowing of the recombination zone is expected as a consequence of increasing triple-charge annihilation with increasing current density. The decrease of the recombination zone width might also be a consequence of a shift of the recombination zone, which is not included in the model. However, the main purpose of the model is the determination of the generation rate G_0.

*bodo79@gmx.net

†Corresponding author: RHF10@cam.ac.uk

[1] J. H. Burroughes, D. D. C. Bradley, A. R. Brown, R. N. Marks, K. Mackay, R. H. Friend, P. L. Burns, and A. B. Holmes, Nature **347**, 539 (1990).

[2] R. H. Friend, R. W. Gymer, A. B. Holmes, J. H. Burroughes, R. N. Marks, C. Taliani, D. D. C. Bradley, D. A. Dos Santos, J. L. Brédas, M. Lögdlund, and W. R. Salaneck, Nature **397**, 121 (1999).

[3] B. H. Wallikewitz, D. Hertel, and K. Meerholz, Chem. Mater. **21**, 2912 (2009).

[4] A. S. Wilson, A. S. Dhoot, A. J. A. B. Seeley, M. S. Khan, A. Köhler, and R. H. Friend, Nature **413**, 828 (2001).

[5] A. Köhler and H. Bässler, Mater. Sci. Eng. R **66**, 71 (2009).

[6] M. A. Baldo, D. F. O'Brien, Y. You, A. Shoustikov, S. Sibley, M. E. Thompson, and S. R. Forrest, Nature **395**, 151 (1998).

[7] G. Schwartz, S. Reineke, T. C. Rosenow, K. Walzer, and K. Leo, Adv. Funct. Mater. **19**, 1319 (2009).

[8] Y. Sun, N. C. Giebink, H. Kanno, B. Ma, M. E. Thompson, and S. R. Forrest, Nature **440**, 908 (2006).

[9] D. Kabra, L. P. Lu, M. H. Song, H. J. Snaith, and R. H. Friend, Adv. Mater. **22**, 3194 (2010).

[10] D. Y. Kondakov, T. D. Pawlik, T. K. Hatwar, and J. P. Spindler, J. Appl. Phys. **106**, 124510 (2009).

[11] S. Mladenovski, K. Neyts, D. Pavicic, A. Werner, and C. Rothe, Opt. Express **17**, 7562 (2009).

[12] M. A. Stevens, C. Silva, D. M. Russell, and R. H. Friend, Phys. Rev. B **63**, 165213 (2001).

[13] S. Gélinas, O. Par, C.-N. Brosseau, S. Albert-Seifried, C. R. McNeill, K. R. Kirov, I. A. Howard, R. Leonelli, R. H. Friend, and C. Silva, J. Phys. Chem. C **115**, 7114 (2011).

[14] C. Rothe, H. A. Al Attar, and A. P. Monkman, Phys. Rev. B **72**, 155330 (2005).

[15] C. Rothe and A. P. Monkman, Phys. Rev. B **68**, 075208 (2003).

[16]C. Rothe, S. M. King, and A. P. Monkman, Phys. Rev. Lett. **97**, 076602 (2006).
[17]S. M. King, M. Cass, M. Pintani, C. Coward, F. B. Dias, A. P. Monkman, and M. Roberts, J. Appl. Phys. **109**, 74502 (2011).
[18]D. Hertel, H. Bässler, R. Guentner, and U. Scherf, J. Chem. Phys. **115**, 10007 (2001).
[19]D. Hertel, Y. V. Romanovskii, B. Schweitzer, U. Scherf, and H. Bässler, Synth. Met. **116**, 139 (2001).
[20]D. J. Pinner, R. H. Friend, and N. Tessler, J. Appl. Phys. **86**, 5116 (1999).
[21]D. J. Pinner, R. H. Friend, and N. Tessler, J. Appl. Phys. **97**, 014504 (2005).
[22]C. Ganzorig and M. Fujihira, Appl. Phys. Lett. **81**, 3137 (2002).
[23]D. Y. Kondakov, J. Appl. Phys. **102**, 114504 (2007).
[24]J. Partee, E. L. Frankevich, B. Uhlhorn, J. Shinar, Y. Ding, and T. J. Barton, Phys. Rev. Lett. **82**, 3673 (1999).
[25]Y. Luo and H. Aziz, Adv. Funct. Mater. **20**, 1285 (2010).
[26]S. Sinha and A. P. Monkman, J. Appl. Phys. **97**, 114505 (2005).
[27]A. S. Dhoot and N. C. Greenham, Adv. Mater. **14**, 1834 (2002).
[28]T. A. Ford, I. Avilov, D. Beljonne, and N. C. Greenham, Phys. Rev. B **71**, 125212 (2005).
[29]C.-L. Lee, X. Yang, and N. C. Greenham, Phys. Rev. B **76**, 245201 (2007).
[30]D. Kabra, M. H. Song, B. Wenger, R. H. Friend, and H. J. Snaith, Adv. Mater. **20**, 3447 (2008).
[31]R. A. Marsh, J. M. Hodgkiss, and R. H. Friend, Adv. Mater. **22**, 3672 (2010).
[32]K. Muellen and U. Scherf, *Organic Light Emitting Devices* (Wiley-VCH, Weinheim, 2005), pp. 171–172.
[33]M. Wohlgenannt, K. Tandon, S. Mazumdar, S. Ramasesha, and Z. V. Vardeny, Nature **409**, 494 (2001).
[34]A. P. Monkman, C. Rothe, and S. M. King, Proc. IEEE **97**, 1597 (2009).
[35]J. B. Birks, *Organic Molecular Photophysics* (John Wiley & Sons Ltd., London, 1975), pp. 381–382.
[36]H. T. Nicolai, G. a. H. Wetzelaer, M. Kuik, a. J. Kronemeijer, B. de Boer, and P. W. M. Blom, Appl. Phys. Lett. **96**, 172107 (2010).
[37]P. W. M. Blom and M. C. J. M. Vissenberg, Mater. Sci. Eng. R **27**, 53 (2000).
[38]H. C. F. Martens, P. W. M. Blom, and H. F. M. Schoo, Phys. Rev. B **61**, 7489 (2000).
[39]W. F. Pasveer, J. Cottaar, C. Tanase, R. Coehoorn, P. A. Bobbert, P. W. M. Blom, D. M. de Leeuw, and M. A. J. Michels, Phys. Rev. Lett. **94**, 206601 (2005).
[40]M. Pope and C. E. Swenberg, *Electronic Processes in Organic Crystals and Polymers* (Oxford University Press, New York, 1999), pp. 164–166.
[41]M. J. Bird, Ph.D. thesis, University of Cambridge, 2010.
[42]D. Kasemann, R. Brückner, H. Fröb, and K. Leo, Phys. Rev. B **84**, 115208 (2011).
[43]L. Sudha Devi, M. K. Al-Suti, C. Dosche, M. S. Khan, R. H. Friend, and A. Köhler, Phys. Rev. B **78**, 045210 (2008).
[44]I. Howard, Ph.D. thesis, University of Cambridge, 2009.
[45]N. C. Giebink, Y. Sun, and S. R. Forrest, Org. Electron. **7**, 375 (2006).
[46]C. M. Ramsdale and N. C. Greenham, J. Phys. D **36**, L29 (2003).
[47]M. Samiullah, D. Moghe, U. Scherf, and S. Guha, Phys. Rev. B **82**, 205211 (2010).
[48]M. A. Baldo, D. F. O'Brien, M. E. Thompson, and S. R. Forrest, Phys. Rev. B **60**, 14422 (1999).
[49]J.-S. Kim, Peter K. H. Ho, N. C. Greenham, and R. H. Friend, J. Appl. Phys. **88**, 1073 (2000).
[50]A. S. Dhoot, D. S. Ginger, D. Beljonne, Z. Shuai, and N. C. Greenham, Chem. Phys. Lett. **360**, 19 (2002).
[51]M. Carvelli, R. A. J. Janssen, and R. Coehoorn, Phys. Rev. B **83**, 075203 (2011).
[52]M. Segal, M. A. Baldo, R. J. Holmes, S. R. Forrest, and Z. G. Soos, Phys. Rev. B **68**, 075211 (2003).
[53]M. Flämmich, J. Frischeisen, D. S. Setz, Dirk M., B. C. Krummacher, T. D. Schmidt, W. Brütting, and N. Danz, Org. Electron. **12**, 1663 (2011).
[54]D. Hertel and K. Meerholz, J. Phys. Chem. B **111**, 12075 (2007).
[55]S. Reineke, K. Walzer, and K. Leo, Phys. Rev. B **75**, 125328 (2007).
[56]S. Larsson and L. Rodriguez-Monge, Int. J. Quantum Chem. **58**, 517 (1996).